Shape-tuned Electrodeposition of Bismuth-based Nanosheets on Flow-through Hollow Fiber Gas Diffusion Electrode for High-efficiency CO_2 Reduction to Formate

*Hesamoddin Rabiee [a], Lei Ge *[b, c], Xueqin Zhang [a], Shihu Hu *[a], Mengran Li [c], Simon Smart [c], Zhonghua Zhu [c], and Zhiguo Yuan [a]*

[a] Advanced Water Management Centre, Faculty of Engineering, Architecture and Information Technology, The University of Queensland, St. Lucia, Queensland 4072, Australia. E-mail: s.hu@awmc.uq.edu.au

[b] Centre for Future Materials, University of Southern Queensland, Springfield Central, QLD 4300, Australia. E-mail: lei.ge@usq.edu.au

[c] School of Chemical Engineering, The University of Queensland, Brisbane, QLD 4072, Australia

* Corresponding Author

KEYWORDS: CO_2 Electrochemical Reduction Reaction, 2D Materials, Hollow Fiber Gas Diffusion Electrodes, Electrocatalysis, Formate Production, Bismuth Electrocatalyst

Abstract

Gas-phase CO_2 electrochemical reduction reaction (CO_2RR) requires advanced gas diffusion electrodes (GDEs) for efficient mass transport. Meantime, engineering catalyst nanostructure and tuning surface wettability are decisive to enhance three-phase interfaces formation. Herein, Bi-based nanosheets are uniformly grown on flow-through Cu hollow fiber GDE (HFGDE) to benefit from the unique shape of HFGDEs, and abundant active surface area of nanosheets. Pulse electrodeposition is used to replenish Bi^{3+} ions in the vicinity of HFGDEs for uniform growth of Bi nanosheets. Further, thermal oxidation of nanosheets not only maximized the active sites and improved surface wettability but also induced Bi/Bi_2O_3 junctions in nanosheets, enhancing formate production via switching the rate-limiting step from the initial electron transfer to hydrogenation. Consequently, a current density of 141 mA cm^{-2} at -1 V vs. RHE with formate faradaic efficiency of 85% and over six times greater catalyst mass activity compared to bulk particle shaped Bi, were achieved, outperforming other reported Bi-based GDEs used for formate production in bicarbonate electrolytes. This comes from less charge-transfer resistance, higher surface roughness, and improved wettability of Bi nanosheets after oxidation. This work represents a facile strategy to engineer efficient HFGDEs as advanced electrode materials for similar electrochemical reactions with low aqueous solubility gas-phase feeds.

1. Introduction

Electrocatalytic CO_2 reduction reaction (CO_2RR) has attracted much attention as a green solution at ambient conditions to deal with the detrimental impacts of CO_2 emission and carbon cycle crisis when coupled with renewable resources [1]. Diverse valuable compounds such as syngas (CO + H_2), ethylene, methane, ethanol, formate, and other C_{2+} products can be obtained from CO_2RR with the collective market size of over 500 Megatonnes per year [2]. Among these products, formate (formic acid) is a key intermediate renewable chemical feedstock and a safe and convenient liquid for hydrogen storage with the possibility of being directly fed to a formic acid fuel cell [3, 4]. Many efforts have been made to improve the efficiency of electrocatalysts to speed up the sluggish kinetics of CO_2RR, and the high selectivity for the desired product(s) [5]. At the same time, the significance of the electrode configuration should not be neglected [6].

To date, the majority of studies examined CO_2RR performance with planar electrodes, where the electrocatalysts are simply coated on glassy carbon or carbon paper and immersed in the CO_2-saturated electrolyte [7]. In this case, CO_2RR cannot be operated at commercially relevant current densities (>200 mA cm^{-2}) [8], due to the poor mass transport of CO_2 from the electrolyte bulk toward the electrode [6]. Gas diffusion electrode (GDE), on the other hand, can be used to continuously feed CO_2 to the reactor and minimize the CO_2 diffusion pathway towards the catalyst, as compared with the planar configuration [9]. GDE guarantees sufficient CO_2 supply which is crucial to maintain the high-rate and selective CO_2RR [10], and also increases the catalytic surface area and enhances the creation of triple-phase interfaces (electrolyte, gas, and catalyst) [9]. Thereby, high selectivities and current densities can be simultaneously obtained, provided that the catalyst nanostructure and surface wettability of GDEs are tuned [3, 11].

Planar GDE, comprising of a carbon-based gas diffusion layer (GDL) and a catalyst layer (CL) facing the electrolyte, is the conventional structure of GDE in which a separate chamber is needed for delivery of the gaseous feed. Despite the advantages of CO_2RR with GDE, carbon-based GDL is prone to flooding due to electro-wetting under cathodic condition or carbonation-derived pore blockage as a result of CO_2 reaction with alkaline electrolytes [12]. This disrupts the gas-liquid interface within the GDE, resulting in intensified hydrogen evolution reaction (HER), and compromising the selectivity of products, especially in high current densities. As a result, most of the emerging gas-fed CO_2 electrolyzers suffer from performance degradation after a few hours of operation [12]. Besides, the fabrication of planar GDEs includes several steps, and several effective parameters need to be tuned for the multiple layers (microporous layer, GDL, and CL) [10], therefore the need for new GDE designs arises.

Hollow fiber gas diffusion electrode (HFGDE) is a new electrode structure with flow-through configuration [13] and abundant surface areas due to its tubular shape and small diameter which allow us to increase the catalyst area without necessarily increasing the cell size [14, 15]. HFGDEs for CO_2RR (Cu-based) was primarily developed by Kas et al. via the industrially viable dry-wet spinning technique using relatively low-purity Cu powders (99%), and obtained at least 1 order of magnitude larger CO formation rate compared to ultrapure nanocrystalline Cu electrodes [15]. Recently, we tuned the selectivity of Cu-based HFGDEs to produce formate via controlled electrodeposition of formate-selective Sn catalyst and improved FE of formate by over two times as compared with the pristine Cu HFGDE [14]. Reviewing the literature shows that Bismuth (Bi) generally exhibits relatively better performance for formate formation than Sn [16]. For example, the overpotential required to achieve the highest formate FE for Bi is around 0.2-0.3 V lower than that for Sn [17], and Bi exhibits reportedly higher FE of formate than Sn, up to 90-100% [18].

Moreover, the nanostructure and morphology of the electrocatalyst play a vital role in determining the catalytic activity and product selectivity [19]. 2D electrocatalysts (nanosheets, nanoflakes) substantially increase electrochemical active surface area (ECSA) and boost the current density of reaction [20, 21]. Another important parameter for electrocatalyst design is surface wettability which can improve the formation of triple-phase interfaces, a key factor to facilitate a sufficient supply of CO_2 reactant to the catalyst surface [11]. Wettability can be enhanced via inducing metal/metal oxide defect sites to boost the catalytic activity and CO_2 adsorption of the nanosheets and improve CO_2RR efficiency [22-24]. Considering these parameters, Bi/Bi_2O_3 nanosheets can provide abundant catalytic active surface area and the desired wettability. Bi/Bi_2O_3 nanosheets have been synthesized via hydrothermal method or indirect electroreduction of Bi precursor templates [25]. These approaches require extreme conditions (e.g., high temperature) with multi-steps which make them undesirable if considered on HFGDEs as can be harmful to the structure of HFGDEs. Thereby, a method of direct deposition of nanosheets at ambient conditions with the ability to control the catalyst morphology and nanostructure is desired. Electrodeposition can be effectively employed for this purpose, besides it benefits the charge transfer between the deposited catalyst and hollow fiber substrate because no binder/ionomer is required [26].

To design advanced HFGDEs via engineering the nanostructure of electrocatalyst and maximizing gas-liquid-solid interface, herein Bi/Bi_2O_3-based nanosheet arrays were directly grown on the Cu HFGDE via facile electrodeposition method. By carefully applying pulse electrodeposition (PE) technique, Bi nanosheets uniformly grew on the outer of Cu HFGDE, while a conventional continuous electrodeposition (CE) technique resulted in a bulky shaped catalyst layer. Furthermore, the catalyst wettability and active surface area were maximized via thermal oxidation at a mild temperature. This resulted in inducing defect sites and rough surface, which also enhanced CO_2RR efficiency due to the formation of stable Bi/Bi_2O_3 junctions. The HFGDE loaded

with Bi-based electrocatalysts outperformed the conventional planar Bi-based GDEs for the production of formate in bicarbonate electrolytes. This research exhibits the design of advanced electrode materials with engineered nanostructure and wettability towards obtaining a commercially relevant CO_2RR rate.

2. Experimental

2.1. HFGDE Fabrication

The Cu-based HFGDE was fabricated via a dry-wet spinning technique, following a thermal calcination/reduction step (Fig. S1), explained elsewhere [14]. In brief, the solution of Cu particles (5-10 μm, 99% purity, Sandvik, UK), Polyethersulfone (PES Ultra son, BASF, Germany) as the binder, and N-methyl-2-pyrrolidone (NMP, Sigma) as the polymer solvent with the respective ratio of 65wt%:26.25wt%:8.75wt% was prepared. Subsequently, it was extruded through a spinneret rig (an outer diameter of 1.9 mm and an inner diameter of 0.7 mm) to the water bath. Deionized water at a flow rate of 20 $ml.min^{-1}$ was pumped through the bore of the spinneret. After 24 h, the "green" fibers were then calcinated in a tubular furnace at 650 °C for 2 h in the air atmosphere to remove the polymeric binder, followed by a reduction at 500 °C for 1 h in the H_2/Ar:20/80 atmosphere (heating/cooling rate of 5 °C/min for all the furnace steps). The HFGDEs were stored under the N_2 atmosphere.

2.2. Electrodeposition of Bi on Cu HFGDE

Electrodeposition of Bi on the Cu HFGDEs was done via two different techniques: pulse electrodeposition (PE) and continuous electrodeposition (CE). The electrodeposition was done in a solution of 33 mM $Bi(NO_3)_3$ (Sigma) and 32 M HCL (Alfa Aesar). The Cu HFGDE was purged by Ar during the electrodeposition to prevent blockage of Cu HFGDE pores. Cu HFGDE was used

as the working electrode. A Bi foil (0.25 mm thickness, 99.9%, Sigma) was used as the anode (sacrifice electrode). The schematic of the electrodeposition cell can be found in our previous study [14]. For electrodeposition of Bi on Cu HFGDE, a three-electrode set-up with an Ag/AgCl reference electrode was used. The potential was kept at -0.2 V vs. Ag/AgCl. For CE technique (CuBi-CE HFGDE), the electrodeposition was carried out at a duration of 30s, 60s, 120s, 240s, and 300s. PE technique (CuBi-PE HFGDE) was done with 1s-on and 5s-off for each cycle at 30, 60, 90, 120, and 150 cycles. The duration of CE and the number of cycles in PE were chosen based on having a continuous covering Bi layer on Cu HFGDE. The adsorbed ions on the HFGDE surface were removed via rinsing the CuBi HFGDEs by deionized water. CuBi-PE HFGDE was further treated for 3h at 220 °C in a tubular furnace under the air atmosphere to fully oxidize Bi to Bi_2O_3 ($CuBi_2O_3$-PE HFGDE). The working temperature of 220 °C was chosen since it is well below Bi's melting point (270 °C), thus ensure the step would not jeopardize Bi nanosheets' shape. Besides, oxidation at high temperatures might affect the electrical conductivity of the Cu substrate, causing more ohmic resistances. The Ar pressure drop (inlet pressure-outlet pressure) was constantly monitored during the electrodeposition, and no significant changes were observed, therefore it can be said that the surface porosity of the HFGDEs was maintained during the electrodeposition [14].

2.3.Material Characterizations

The cross-section and surface of flow-through hollow fiber gas diffusion electrodes were inspected by field emission scanning electron microscopy (FESEM, JOEL-7100F). The elemental mapping was done by an energy dispersive X-ray analyzer (EDX). The nanostructures of the deposited Bi on the electrode surface were analyzed by high-resolution Transmission electron microscopy (HRTEM, Hitachi HF5000, Japan). The crystalline structures of the bulk electrodes were examined

by X-ray diffraction (XRD, Rigaku SmartLab, Cu Kα (λ = 1.5405 Å) radiation source, Japan). X-ray photoelectron spectroscopy (XPS) was carried out to analyze the surface valence state and surface compositions of the HFGDEs. XPS was conducted on a Kratos Axis ULTRA XPS with a monochromatic Al Kα radiation source (1486.6 eV) at 15 kV (10 mA) and a hemispherical electron energy analyzer (165 mm). CASA® software was used to analyze the XPS data, calibrated to the C 1s signal at 284.8 eV as the reference. The water contact angles of HFGDEs were measured at 25 ˚C by dropping 1 µl of DI water on the outer surface of HFGDE. After 10s when the DI water was stabilized on the surface, pictures were taken by custom-made sessile drop equipment at least in three different spots for each sample. The weight of deposited Bi was calculated by weighting Cu HFGDE before and after electrodeposition (once the HFGDEs are completely dried overnight). The thickness of Bi nanosheet was measured using Asylum Research Cypher S atomic surface microscopy (AFM). The Bi nanosheets grown on the Cu HFGDEs were carefully exfoliated by a doctor blade and were dispersed in ethanol. After 1h ultrasonication in a bath, one droplet of the solution was cast on a Mica substrate and was let to dry overnight before AFM analysis.

2.4. CO_2 Electrochemical Reduction and Analysis of Products

The electrochemical reaction of CO_2 was analyzed in an H-cell 3-electrode reactor with the hollow fibers as the working electrode [15]. The reference electrode was an Ag/AgCl electrode (3M NaCl, BASi, USA). A Luggin capillary (filled with 3M NaCl) was used to place the reference electrode close to the HFGDE. The counter electrode (Pt wire) was used for the anodic water splitting (O_2 evolution). The HFGDE length (cathode) was 4-4.5 cm for all the samples. A proton conductive membrane (Nafion 117 from Fuel Cell store) was used to separate the anode and cathode chambers. The cathode potentials were controlled by a potentiostat (BioLogic VMP3) for chronoamperometry, cyclic voltammetry (CV), and linear scanning voltammetry (LSV). 0.5 M

$KHCO_3$ solution was used as both catholyte and anolyte. The following equation was used to convert potentials to the reversible hydrogen electrode (RHE) scale:

$$E\ (V\ vs.\ RHE) = E\ (V\ vs.\ Ag/AgCl) + E^{o}_{Ag/AgCl} + 0.0591\ pH$$

$E^{o}_{Ag/AgCl}$ is 0.209 for Ag/AgCl electrode with 3M NaCl. To feed the reactor with CO_2 (99.99%, Coregas, Australia), one end of the Cu hollow fiber was sealed with epoxy, and CO_2 was purged through the other end, flowing through the porous wall (flow-through configuration [13]). Magnetic stirring was applied throughout the experiments to improve mass transport of CO_2 and maintain homogeneous electrolyte/products concentrations near the hollow fibers. To condition the HFGDEs, CV scans between -1 and -1.6 V vs. Ag/AgCl (100 mV s^{-1}) were performed for HFGDEs, followed by a pre-reduction at -1.6 V vs. Ag/AgCl under CO_2 purging for 30 min to obtain a stable current [27]. A pH meter probe (Metrohm LL Unitrode PT1000) was used to measure the catholyte pH.

Electrochemical impedance spectroscopy (EIS) measurements were carried out from 100 kHz to 0.1 Hz with a perturbation signal of 10 mV amplitude at -1.0 V vs. RHE. The electric double-layer capacitance (C_{dl}) of hollow fibers was calculated via CVs over a 0.1 V electrochemical window near the open-circuit voltage (OCV) where no faradaic reaction occurs, at various scan rates (20 to 100 mV/s). The double-layer capacitances were calculated via:

$$C_{dl} = J/(\frac{dV}{dt}) \qquad (1)$$

where J is the current density in the center of 0.1 V electrochemical window, $\mathbf{C_{dl}}$ is the capacitance, and $\frac{\mathbf{dv}}{\mathbf{dt}}$ represents the CV scan rate. EIS and C_{dl} were performed while purging the electrolyte with CO_2.

The LSV of HFGDEs was acquired from -0.4 V to -1.4 V vs. RHE at a 5 mV s^{-1} sweeping rate. Before LSV, CO_2 was purged for at least 30 min through the hollow fibers to the electrolyte to reach pH equilibrium, and it continued during the test. LSV was also performed while purging Ar (99.9%, Coregas, Australia) in the hollow fibers to analyze changes in linear scanning voltammetries in the CO_2-free catholyte. The geometric surface area was used to normalize the reported current densities. For all the experiments, the flow of gases (CO_2 or Ar) was set at 20 ml/min by a mass flow controller (Bronkhorst, ± 1% resolution, Netherlands).

Chronoamperometry of HFGDEs was carried out for 60 min at various applied potentials of -0.7 to -1.2 V vs. RHE (0.1 V intervals). After 30 min of applying potential and reaching the steady-state condition, liquid and gas samplings were carried out to determine the faradaic efficiency (FE) of products. CO_2 purging (20 ml/min) through the HFGDEs carried on during chronoamperometry. The formate production was measured by HPLC (high-performance liquid chromatography, Shimadzu Corporation, Japan). A Hi-Plex H column (8 µm, Agilent Technologies, Inc.), 7.7 x 300 mm with a UV-Vis detector (SPD-20A/20AV) was used in HPLC. The formate faradaic efficiency was calculated by considering the total passed charge and the charge consumed for the formate production, via the following equation:

$$FE_{formate} = \frac{2Fn_{formate}}{Q} \quad (2)$$

where $n_{formate}$ is the mole of produced formate (by HPLC), F is Faraday's constant (96485 C mol^{-1}), and Q is the total charge during the experiment (from time of sampling and the measured current).

Gaseous product analysis was done in a gas chromatograph (GC, Shimadzu 2014). To separate the gases, a packed column (ShinCarbon ST 80/100, 1/8" OD, 2 mm ID, Silico, Restek) was used. H_2

was detected by a thermal conductivity detector (TCD) and for the detection of other gaseous products, a flame ionization detector (FID) was used. The following equation was used to determine the faradaic efficiency of gaseous products:

$$FE_i = \frac{e_i \times F \times P \times V \times X_i}{J \times R \times T} \times 100 \quad (3)$$

where e_i is the required electron transfer production of one mole of gaseous products (e is 2 for H_2 and CO), V represents the effluent volumetric gas flow rate (measured by a digital flowmeter), P is atmospheric pressure (101.3 kPa), J is the total current recorded by the potentiostat, and X_i is the concentration of each gas in the outlet flow, detected by GC.

For the flow-type reactor, chronoamperometry analysis was done by pumping electrolytes (0.5 $KHCO_3$) through the anodic and cathodic chambers (10 ml/min) by peristaltic pumps, while CO_2 was purged through the hollow fibers at 20 ml/min. The catholyte outlet went to a water trap bottle to separate gas (including unreacted CO_2 and gas products) from the liquid (electrolyte and produced formate). Liquid and gas samplings to calculate the faradaic efficiency of the products were done every hour for a period of 24 h. An anion exchange membrane (Fumatech FAA-3-PK-130) was used to separate the cathode and anode chambers. The measurements of faradaic efficiency and electrochemical tests were repeated for at least three times and the average values are reported.

3. Results and Discussion

3.1. Preparation and Characterization of Bi-deposited HFGDEs

The Cu HFGDE was prepared via dry-wet process followed by a sintering step, and we previously observed that they have enough stability for handling and as an electrode for electrochemical

experiments [14]. The cross-sectional SEM images showed a uniform wall thickness for the Cu HFGDE (150-160 μm) with a highly porous structure (Fig. S2a). This facilitates the CO_2 transport to the electrolyte/catalyst interface to supply sufficient CO_2 for the reaction, while the selective reaction occurs on the catalyst layer on the HFGDE surface with controllable active sites. It was reported by Kas et al. that the CO_2RR performance (current density and FE of CO) depended on the flow rate of CO_2 flow rate through the Cu hollow fiber when the flow rate was below 20 ml/min, but remained steady at higher flow rates, indicating that most active sites were involved in CO_2RR at a high flow rate [15]. In our previous work [14] and herein, we accordingly chose a flow of 20 ml/min to allow us to compare our performance with other studies, and to also ensure that the reaction was not limited by the lack of CO_2 supply.

The energy dispersive X-ray (EDX) spectra showed clean peaks attributed to the precursor Cu (Fig. S3), confirming that the polymer binder is completely removed from the HFGDE structure, and the existence of Bi peaks after electrodeposition (Fig. S3b). The deposition of Bi via electrodeposition occurs on the outer layer of porous Cu HFGDE, and CO_2 which is purged through the lumen side is reduced to formate on Bi catalyst surface, as schematically shown in Fig. 1a. As can be seen in Fig. 1b, Cu hollow fibers with length up to 10 cm were fabricated, and a length of around 4-5 cm was used for electrochemical tests. It was observed that the color of Cu HFGDE changed to grey after Bi electrodeposition (Fig. 1b and Fig. S2 b1-b3). Controllable growth of 2D structure materials via electrodeposition depends on multiple parameters such as electroplating solution, additives, electrodeposition method (constant or pulse), applied potential/current density, and the duration of electrodeposition [28, 29]. These parameters in addition to the effect of substrate, need to be tuned to effectively grow 2D materials via electrodeposition [18, 19, 30]. Herein, Cu HFGDE with a highly rough and porous surface was used as the substrate, and it was observed that continuous electrodeposition (CE) did not result in

the growth of Bi nanosheets, and the formation of bulky shape Bi was seen, as schematically shown in Fig. 1c. However, pulse electrodeposition (PE) technique, comprising of multiple "on" and "off" cycles, led to the growth of uniform 2D Bi on the outer of Cu HFGDE (Fig. 1d).

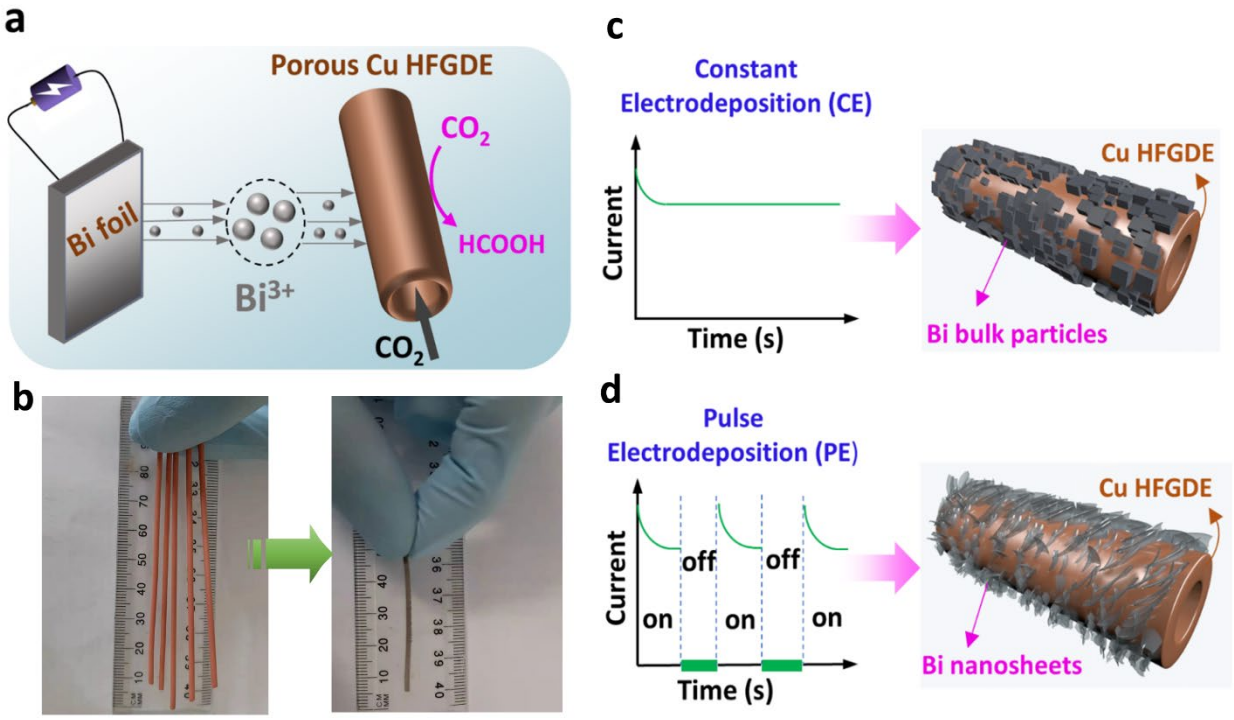

Fig. 1. a) Schematic of Bi electrodeposition on the outer side of flow-through Cu hollow fiber GDE to reduce CO_2 to formate; **b)** Images of Cu hollow fiber before (left) and after (right) Bi electrodespotition; Illustration of Bi deposition on Cu HFGDE from **c)** constant and **d)** pulse electrodeposition, respectively, and the corresponding nanosheet and bulky shape deposited Bi layers.

The difference between CE and PE methods is that Bi^{3+} ion concentrations trend within the vicinity of the Cu substrate. When CE was carried out for 5s, small nanosheets were observed on the surface of the Cu HFGDE (Fig. S4). However, with longer deposition times, these small nanosheets do not grow accordingly, and after 30s, 60s, 120s, 240s, and 300s, bulky pieces cover the HFGDE surface (Fig. S5 a1-a5). Therefore, after 300s of CE (CuBi-CE HFGDE), it is covered by a layer of Bi after 300s electrodeposition (Fig. 2a2 and 2b2 vs. Fig. 2a1 and 2b1), and EDX mapping confirms no significant penetration of Bi into the Cu HFGDE walls during

electrodeposition (Fig. 2 b2, inset). This is because Bi^{3+} ions were continuously consumed and deposited on the substrate during CE, therefore the formation of a concentration polarization of Bi^{3+} ions in the proximity of the electrode was inevitable [29]. As a result, small nanosheets on the HFGDE did not continue to grow due to the lack of sufficient Bi^{3+} ions [18].

Pulse electrodeposition (PE) technique, on the other hand, can be used as an effective way to replenish Bi^{3+} ions to the diffusion layer. Pulse electrodeposition lowers the concentration gradient from the bulk electroplating solution to the electrode surface [28]. In this study, a 1s pluse-on and 5 s pulse-off PE cycle were applied. During the short 1 s pulse-on, adequate Bi^{3+} ions were available in the diffusion layer and it allowed the small nanosheets to grow, while during the 5 s pulse-off, Bi^{3+} ions moved towards the diffusion layer to replenish it for the next pulse-on time [28]. Therefore, after 150 cycles of PE (CuBi-PE HFGDE), Cu substrate was fully covered by Bi nanosheets (Fig. 2a3 and 2b3). The length of CE technique and number of PE cycles was based on having a covering Bi layer was observed in SEM images for both CE (Fig. S5 a1-a5) and PE techniques (Fig. S5 b1-b5), and XPS peaks regarding Cu substrate disappeared (as shown later).

The short 1 s pulse-on during PE ensured that no substantial reduction of the concentration of Bi^{3+} ions occurs in the vicinity of the Cu HFGDE surface. It can be said that during the 1 s pulse-on time**,** Bi^{3+} ions were seeded on the Cu HFGDE surface, and then seeding/growing cycles with access to sufficient Bi^{3+} ions continued in every cycle to uniformly grow nanosheets ((Fig. 2a3 and 2b3)) [28]. However, during CE, seeding occurred in the initial seconds of the deposition, but uniform growth was interrupted due to insufficient Bi^{3+} concentration in the proximity of Cu HFGDE. After 90 cycles of PE (Fig. S6), both small and large nanosheets existed on Cu HFGDE surface, and the small nanosheets continued to grow via seeding-growing till the last cycle. In this way, Bi nanosheets were uniformly grown and tightly cover the Cu HFGDE substrate (Fig. S7).

The surface pores are visible in the SEM images of different HFGDEs with a size of 1-3 μm (Fig. 2a1-2a4), confirming that purging argon gas through hollow fiber lumen during the electrodeposition maintained the surface porosity of Cu HFGDE [14].

The surface area provided by Bi nanosheets for electrochemical reactions can be further maximized by the formation of oxidation-induced defects via thermal treatment [31]. Therefore, the HFGDEs prepared were treated with thermal oxidation at 220 °C for 3h. Induced abundant surface defect states on the nanosheets were observed by comparing Bi nanosheets before (Fig. 2c1) and after (Fig. 2c2) thermal treatment. The thermal treatment well under Bi melting point did not alter the nanosheets shape, which remained vertically aligned (Fig. 2a4, 2b4). The nanostructures and defects created on the nanosheets result in a higher density of low-coordinated sites such as corners and edges, and their high-curvature results a high electric field, leading to active surface area for electrocatalytic reactions and achieving higher current densities [23, 32]. Moreover, adsorption of CO_2 can be facilitated on the oxygen-deficient surface of metal oxides,[33] therefore more active sites are available for CO_2RR on the surface of Bi_2O_3 nanosheets [22-24].

In addition, the creation of surface defect sites after oxidation enhances the water wettability of nanosheets [34]. The contact angle measurement exhibited improvement in surface hydrophilicity of CuBi-PE HFGDE after thermal oxidation (Fig. S8), confirming the efficacy of thermal treatment to maximize three-phase interface formation. The wettability of the electrocatalyst layer is a vital factor affecting the two-phase interface between solid catalyst and CO_2-saturated electrolyte and CO_2RR efficiency [11]. For CO_2RR in an aqueous electrolyte, the dry electrocatalyst is not active and improved wettability of the catalyst layer results in the extension of the solid-liquid interface and stabilization of interfacial gas concentration [11]. The obtained Bi nanosheets showed a

thickness of ~ 20 nm, as seen in the AFM image and the corresponding height profile (Fig. 2d1 and 2d2). A similar thickness for Bi nanosheets was also seen in high-resolution SEM images (Fig. S9). Moreover, it was observed that nanosheets thickness increased after thermal treatment (Fig. S9a2 and b2).

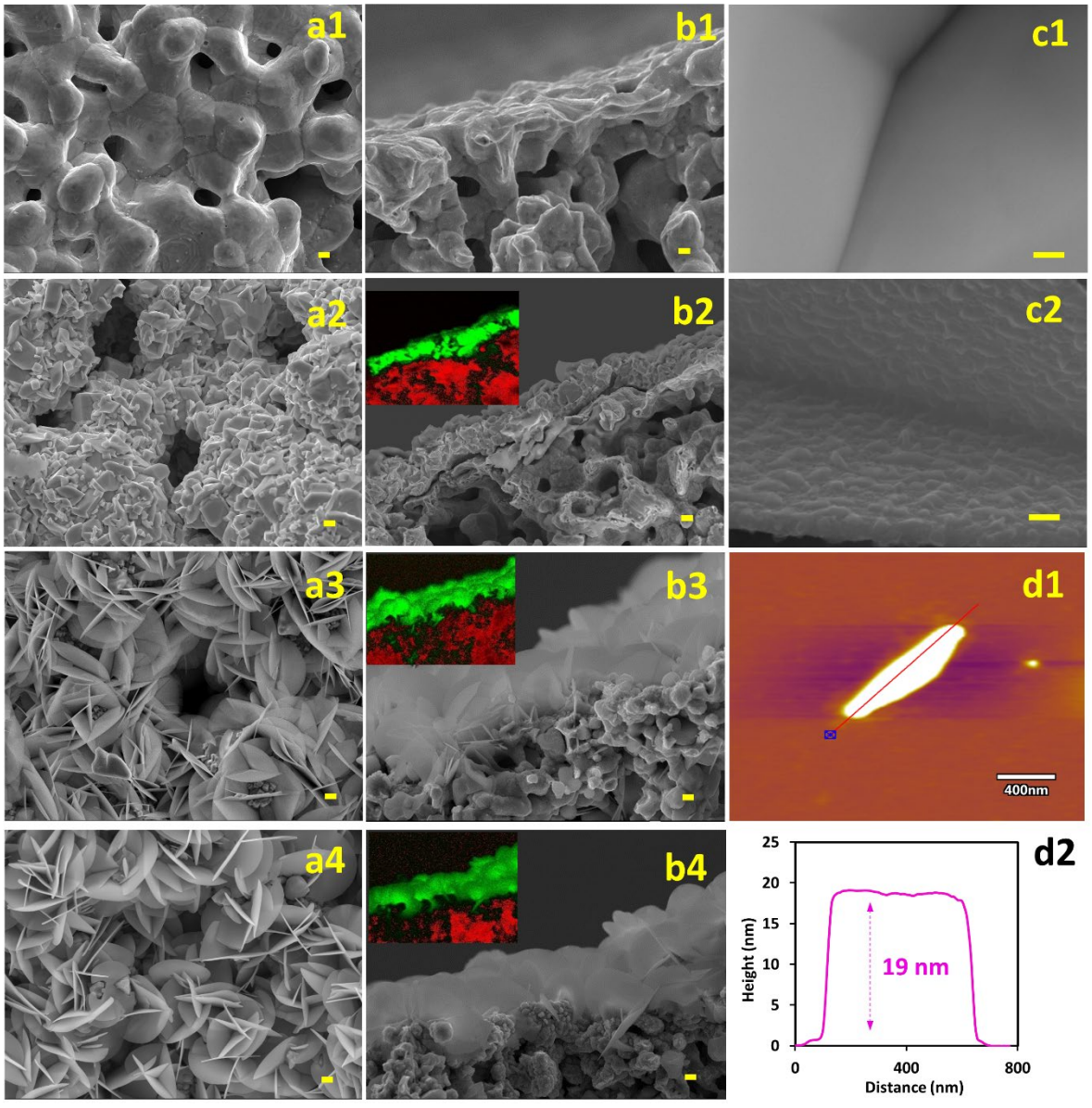

Fig. 2. Surface SEM images of HFGDEs **a1)** Cu, **a2)** CuBi-CE, **a3)** CuBi-PE, **a4)** $CuBi_2O_3$-PE; Cross-section SEM images of HFGDEs **b1)** Cu, **b2)** CuBi-CE, **b3)** CuBi-PE, **b4)** $CuBi_2O_3$-PE; High-resolution SEM images of **c1)** Bi nanosheets, **c2)** Bi_2O_3 nanosheets; **d1)** AFM image and **d2)** height profile of Bi

nanosheets of porous Cu hollow fiber. Insets in b2-b4 are the corresponding cross-section EDX mapping of SEM images, red represents Cu, green represents Bi. (scale bar: 1 μm for a, b; 100 nm for c1 and c2).

X-ray diffraction (XRD) patterns of Cu HFGDE, CuBi-CE, CuBi-PE, and $CuBi_2O_3$-PE can be seen in Fig. 3a. For all the samples Cu peaks regarding Cu (111), Cu (200), and Cu (220) tissues were observed. After Bi electrodeposition, new peaks attributed to the Bi (012), Bi (104), Bi (110), Bi (024), Bi (116), and Bi (112) planes could be observed for CuBi-PE and CuBi-CE HFGDEs, with the highest diffraction peak at around 27.1° corresponding to Bi (012) rhombohedral structure. The XRD pattern of Bi nanosheets shows the higher intensity of (012), (110), and (104) peaks for PE method. It confirms that Bi nanostructures obtained via PE method possess a higher degree of crystallinity as compared with the CE method. No obvious oxide peaks were observed, confirming the formation of metallic Bi on Cu HFGDEs. As to the $CuBi_2O_3$-PE HFGDE, the XRD peaks of Bi were replaced with the ones related to Bi_2O_3, and the strongest peak was seen at around 27.9°, ascribed to Bi_2O_3 (201) plane. It was seen that after 1h and 2h of treatment, Bi was partially oxidized and there was a combination of Bi and Bi_2O_3 peaks (Fig. S10). However, after 3h of oxidation, peaks attributed to Bi disappeared from the XRD spectra, indicating complete conversion of Bi to Bi_2O_3. After 3h oxidation in air at 220 °C, no XRD peaks attributed to Cu_2O or CuO were observed (Fig. 3a), as complete oxidation of Cu occurs at temperatures higher than 300 °C and longer oxidation time [35]. This is favorable as complete oxidation of Cu substrate may cause an additional electron transfer resistance from the Cu substrate to the deposited Bi layer.

The surface chemistry and oxidation state of the HFGDEs were probed via XPS. As can be seen in the XPS surveys of the HFGDEs before and after Bi deposition (Fig. S11), the characteristic peaks of Cu 2p become weaker with longer durations of CE or more cycles of PE. The peaks of Cu 2p disappeared after 300s of CE and 150 cycles of PE (Fig. 3b) as the Bi layer tightly covered the Cu HFGDE surface as seen in EDX element mapping (Fig. 2b3). While XRD shows that Bi

was mainly in the zero-valence state (Bi^0) for CuBi-PE and CuBi-CE HFGDEs (Fig. 3a), Bi^{3+} was the dominant phase detected on XPS (peaks at 159 eV and 164 eV), and two small peaks at around 157 eV and 162 eV were spotted for Bi^0 (Fig. 3c) [30]. The presence of Bi^{3+} was related to the inevitable oxidation of Bi when exposed to air [33]. For $CuBi_2O_3$-PE, a complete absence of metallic Bi^0 peaks was observed and Bi 4f spectra were fitted by two sharp peaks attributed to Bi^{3+}. The oxidation state of the Bi-based HFGDEs was further elucidated by the deconvolution of O 1s spectra to three peaks (Fig. 3d). The peaks at ~529.3 eV and 530.8 eV were attributed to Bi-O-Bi and Bi−OH lattice bonds, respectively. [28] In addition, a weak peak was found at ~532.5 eV, ascribed to the adsorbed oxygen on HFGDEs surface. Bi-O-Bi / Bi−OH ratio, which was 0.9 for CuBi-PE HFGDE, increased substantially to 1.7 after oxidation which corresponds to well-defined formations of Bi-O structure in $CuBi_2O_3$-PE HFGDE [25]. By considering XRD and XPS results, it can be concluded that the Bi catalyst bulk was mainly in the zero-valence state (Bi^0), while Bi^{3+} was the dominant state on the surface. However, for $CuBi_2O_3$-PE HFGDE, Bi^0 was completely converted to Bi^{3+}.

To further investigate the material properties of the synthesized Bi nanostructures, the crystal structures of the deposited Bi were investigated by high-resolution TEM (HRTEM). As it can be seen in Fig. 3e for CuBi-CE and and S11a for CuBi-PE, several lattice strips were found in the Bi deposited layer which agrees with the XRD results, confirming the polycrystalline structure of the deposited Bi. For the CuBi-CE and CuBi-PE HFGDEs prepared, lattice stripes with d-spacing of 0.33 nm and 0.23 nm, attributed to (012) and (110) planes of Bi, respectively, were observed. For the case of $CuBi_2O_3$-PE HFGDEs, lattice stripes with d-spacing of 0.32 nm were observed, which could be assigned to the (201) plane in accordance with the XRD results (Fig. 3a).

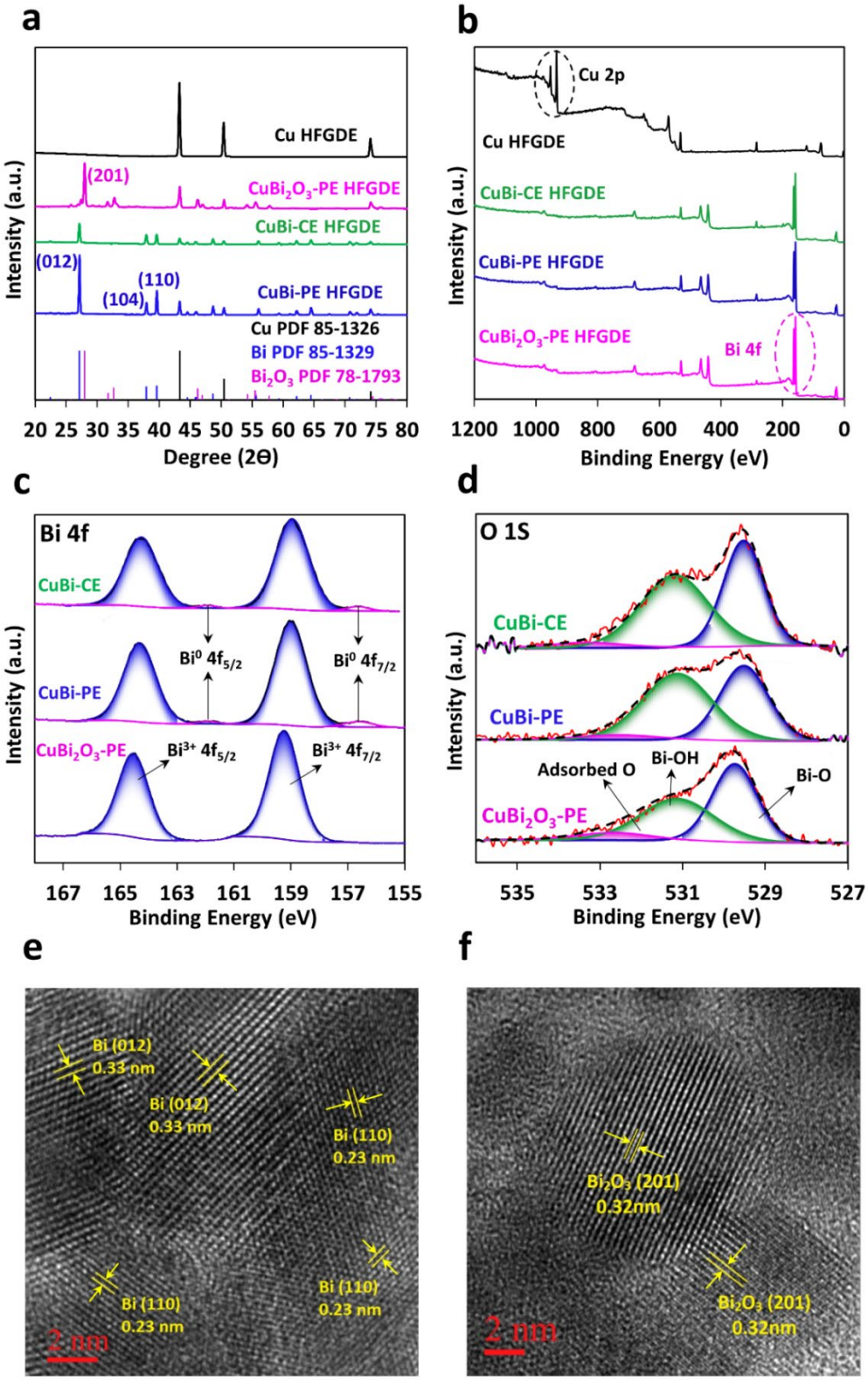

Fig. 3. a) XRD patterns of HFGDEs; **b)** XPS spectra of HFGDEs; high-resolution XPS Spectra of **c)** Bi 4f and **d)** O 1s; high-resolution TEM images of **e)** Bi nanosheets, **f)** Bi_2O_3 nanosheets.

3.2. CO_2 Electrochemical Reduction

The CO_2RR performances of the fabricated HFGDEs can be seen in Fig. 4. The HFGDEs had linear scanning voltammograms with a trend of lower current densities at less negative potentials followed by an increase of current densities at higher overpotentials where CO_2RR and hydrogen evolution reaction (HER) takes place (Fig. 4a). The current densities were particularly higher for the CuBi-PE and $CuBi_2O_3$-PE HFGDEs, owing to the substantially larger surface area available for electrochemical reactions. This was confirmed by measuring the electric double-layer capacitances (C_{dl}) via running cyclic voltammetry (CV) at different scan rates (Fig. S13). As shown in Fig. 4b, C_{dl} increases after Bi deposition on Cu HFGDE, and C_{dl} for CuBi-PE and $CuBi_2O_3$-PE HFGDEs were 3.3 and 5.2 times higher than that for CuBi-CE. The sharp shape of 2D nanosheets and rough surface of $CuBi_2O_3$-PE HFGDE, comprising nanostructures and defects smaller than 50 nm (Fig. 2c2), are likely the reasons for the highest C_{dl} among other HFGDEs. In addition, it was seen in Fig. 4a that the current densities were substantially higher for CO_2 as the feed, as compared with Ar through the HFGDEs. The current densities observed with Ar feeding were related to the hydrogen evolution reaction, whereas upon feeding with CO_2, CO_2RR occurred and competed with HER. The higher current density with CO_2 feeding implies more favorable CO_2RR over competitive HER on Bi-based HFGDEs [16].

Electrochemical impedance spectroscopy (EIS) at -1 V vs. reversible hydrogen electrode (RHE) was applied to probe the kinetics of electron transfer, which showed similar spectra for HFGDEs but with different impedance arcs size (Fig. 4c). The high-frequency intercepts on the real axis (X-axis) (lower Ω) correspond to the ohmic resistances of electrolyte solutions, which were relatively similar for various HFGDEs due to having identical electrolyte, cell components, and conditions [16]. Therefore, the distances between low-frequency and high-frequency intercepts of EIS spectra

on the real axis represent the charge-transfer resistance of the reduction reactions at the specified potential [36]. Cu and CuBi-CE HFGDEs showed similar resistances, while CuBi-PE and $CuBi_2O_3$-PE HFGDEs had smaller arcs sizes as compared with other HFGDEs, therefore lower charge-transfer resistance. The lowest charge-transfer resistance for $CuBi_2O_3$-PE HFGDE confirms that it goes through a high-efficiency catalytic process during CO_2RR [16]. The existence of well-connected nanosheets promotes the electronic conductivity, increases the charge density on the nanosheets, and decreases charge-transfer resistance, resulting in a faster rate of electron transfer from Bi_2O_3 nanosheets to CO_2 [37]. In addition, enhanced contact between the nanosheets surface and the electrolyte after oxidation and inducing crystalline Bi-O structure contributed to less charge-transfer resistance on Bi_2O_3 nanosheets [33]. The improved charge transfer indicates that faster electrochemical reduction occurs on $CuBi_2O_3$-PE HFGDE and this is in accordance with the results observed in Fig. 4a where $CuBi_2O_3$-PE HFGDE exhibited a higher current density compared to other HFGDEs.

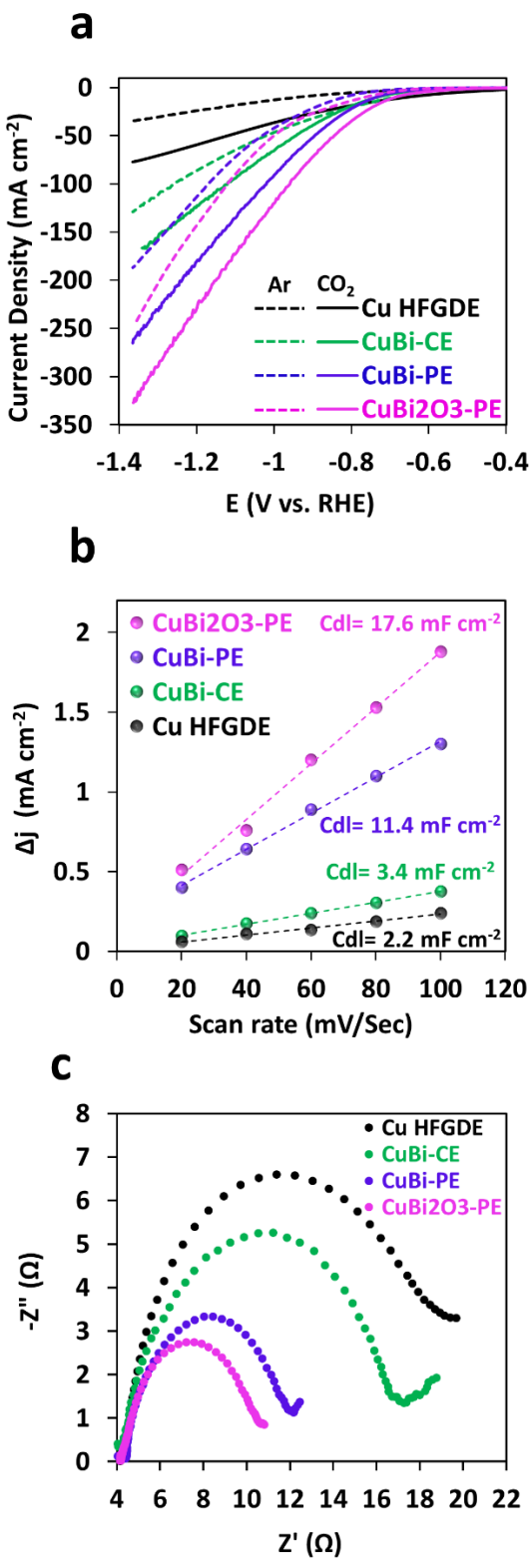

Fig. 4. a) linear scanning voltammograms (LSV) with CO_2/Ar purring through the HFGDEs; **b)** Charging current density differences (Δj) vs. CV scan rates to calculate double-layer capacitance (C_{dl}) of HFGDEs; **c)** Nyquist plots to evaluate electron resistance behavior of HFGDEs.

To analyze the efficiency of the fabricated HFGDEs to selectively reduce CO_2 to formate, chronoamperometry experiments were done over 1 h period at potentials between -0.7 V to -1.2 V vs. RHE with 0.1 V intervals. The current densities observed for all the HFGDEs in the one-hour period were stable with negligible changes (Fig. S14). Analyses of the gas and liquid samples during chronoamperometry confirmed that formate was the only liquid product detected via HPLC, while H_2 and CO were detected in gas samples. The total FE of formate, H_2, and CO was 90-100%, including a small FE of CO (4-5%) for Bi-based HFGDEs (Fig. S15). The highest FE of formate was seen at -0.9 to -1.1 V vs. RHE (Fig. 5a), which has been observed as the common potential window on Bi-based electrocatalysts for CO_2RR to formate [36, 38]. Besides, this exhibits 0.2 V lower overpotential as compared with our previous study on Sn-based HFGDEs for formate production (-1 V for Bi vs -1.2 V for Sn). Therefore, less energy input is required for Bi-based HFGDEs [14]. No hydrocarbons or alcohols were detected from the Bi coated HDGDEs, confirming that the Cu substrate was unlikely to be effective in CO_2RR. It is known that Cu produces several compounds during CO_2RR [39], and previously we observed FE of formate can be as high as 28% for the Cu HFGDE [14]. It has been reported that Bi inhibit HER and is mainly selective to formate during CO_2RR [40]. The hydrogen adsorption free energies at Bi surface is high, based on density functional theory (DFT) calculation [41], therefore Bi has a reduced catalytic activity for HER, and is selective for the production of formate rather than CO. Also, Bi has a relatively low heat of fusion, therefore the adsorption of radical $CO_2^{\bullet-}$ on the Bi surface is weak, leading to fast reaction with H_2O and production of formate [42].

2D nanosheets obtained by PE technique have several advantages over random shape electrocatalyst from CE. Firstly, the edge site of 2D nanosheets lowered the barrier of CO_2 adsorption and formation of COOH* intermediate, which is required for the selective production of formate [18]. These active sites were even more abundant on the surface of $CuBi_2O_3$-PE

HFGDE, due to the substantially rougher surface of nanosheets after oxidation (Fig. 2c2). In addition, high-curvature structures concentrate the electric field, which increases electrolyte cation and consequent CO_2 concentration in the vicinity of the catalyst [32]. It was reported that the electron concertation on the edge sites of nanosheets becomes higher as nanosheets become thinner. For relatively thin nanosheets (thickness ≤ 50 nm), the electric field is substantially more intense than thicker ones, such as 500 nm [18]. Here, it was seen that the deposited nanosheets had a thickness of around 20 nm (Fig. 2d2), leading to a higher local K^+ concentration promoted by the electric field. The higher electric concentration on the edge of nanosheets provided a driving force to move charges from the catalyst to the electrolyte, resulting in a higher current density for the HFGDEs with nanosheets. Further, wettability enhancement of Bi nanosheets after oxidation regulated the reaction sites, resulting in the highest FE of formate in $CuBi_2O_3$-PE, as compared with other HFGDEs. This is because the active sites on Bi_2O_3 nanosheets are catalytically effective when in good contact with CO_2-saturated electrolyte [11], similar to the effect of ionomer coating to boost surface wettability and extending three-phase reaction interface [43]. This wettability effect along with improved adsorption of CO_2 due to the presence of Bi-O [22, 33], effectively maximizes the formation of triple-phase interface and formate production.

The partial current densities of formate for the HFGDEs showed a substantial increase for $CuBi_2O_3$ HFGDE due to both higher FE of formate and higher current density compared to other HFGDEs. As we can see in Fig. 5b, with the increase of applied potentials, the partial current densities for all HFGDEs increased. Cu HFGDE presented a partial current density of around 12 mA cm^{-2} at -1 V vs. RHE. This value increased to 45 mA cm^{-2} for CuBi-CE HFGDE and 74 mA cm^{-2} for CuBi-PE HFGDE. However, the highest partial current density was witnessed for $CuBi_2O_3$-PE HFGDE with over 100 mA cm^{-2}. This was owing to the synergetic effect of 2D materials and enhanced Bi-O structure to boost both formate FE and current density. We observed the highest ECSA for the

$CuBi_2O_3$-PE HFGDE owing to the presence of nanostructure roughness and defects on the surface of nanosheets, which was consistent with the formate partial current density. Conspicuously, Bi nanosheets showed substantially better performance when the partial current density of formate was mass-normalized based on the mg of the deposited electrocatalyst. As can be seen in Fig. 5c, mass-normalized formate partial current density ($j_{Formate}$) for HFGDEs with nanosheets was considerably higher, and $CuBi_2O_3$-PE HFGDE exhibited over six times higher mass activity as compared with CuBi-CE HFGDE. This comes from the morphologic advantages of 2D nanosheets, which provide a much more active surface area, with less catalyst loading. Therefore, the amount of required catalyst can be effectively minimized by altering the electrocatalyst morphology, which is a favorable parameter, particularly for expensive electrocatalysts [44]. The mass-normalized partial current density of formate achieved here outperformed other high-performance state-of-art Bi-based electrocatalysts for formate production from CO_2RR [1, 22, 25].

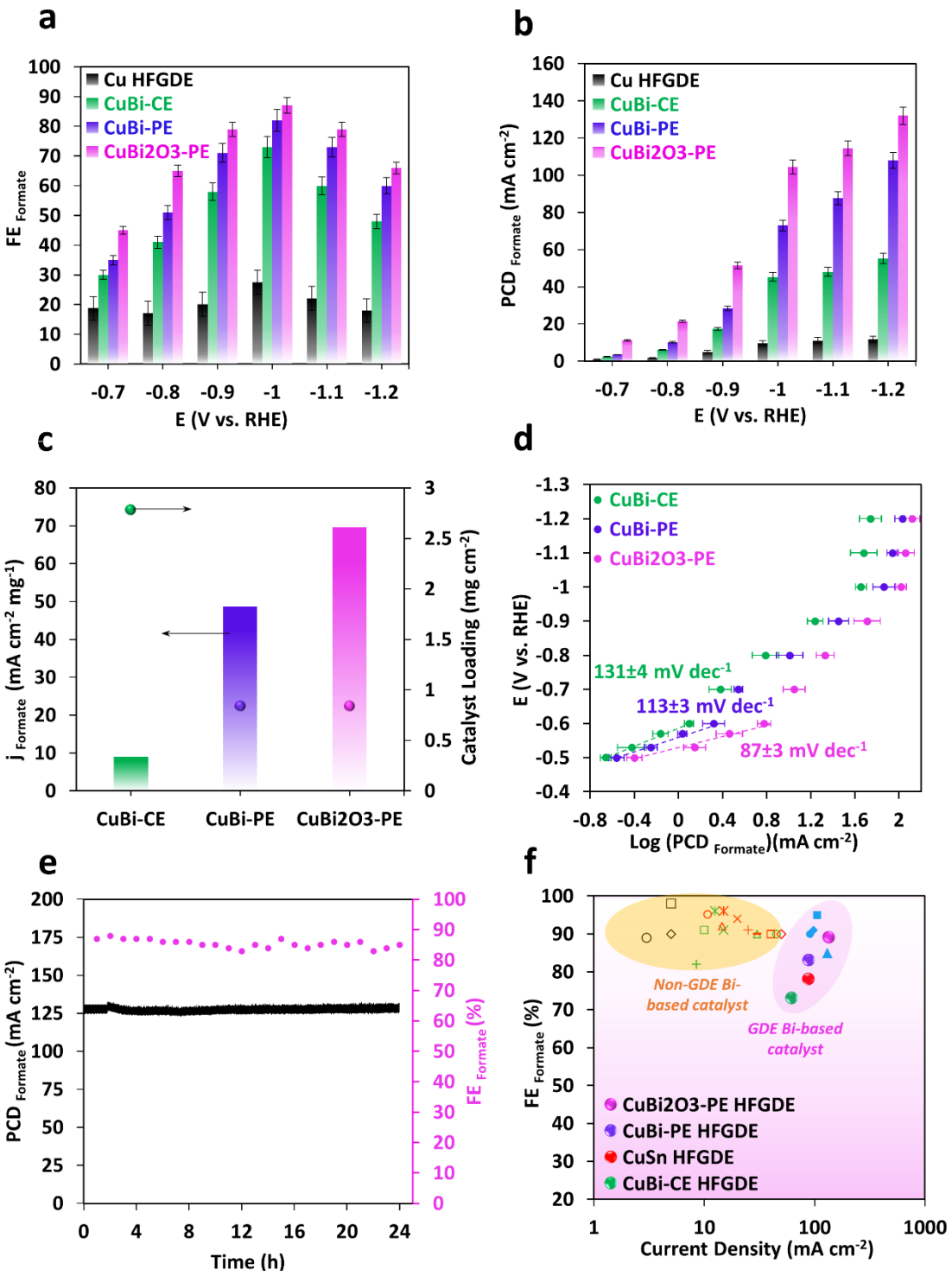

Fig. 5. a) FE and **b)** partial current density of formate for various HFGDEs as a function of potential from -0.7 to -1.2 V vs. RHE; **c)** Mass-normalized formate partial current density at -1 V vs. RHE and catalyst loading of various Bi-based HFGDEs; **d)** Tafel plots of formate for Bi-based HFGDEs; **e)** FE and formate partial current density for 24 h stability test in a flow-type reactor with $CuBi_2O_3$-PE HFGDE at -1.0 V vs. RHE; **f)** CO_2RR performance comparison of Bi-based HFGDEs with other Bi-based non-GDE electrodes and GDEs for formate production in bicarbonate electrolytes (more details in Table S1).

The mechanism of formate formation on Bi and Bi_2O_3 electrocatalysts follows different pathways [33]. A commonly accepted mechanistic pathway for CO_2RR to formate follows 4 steps as illustrated in steps (1) to (4) [4, 42]:

$CO_2(g) \rightarrow CO_2*(ads)$ Step (1)

$CO_2*(ads) + e^- \rightarrow CO_2*^-(ads)$ Step (2)

$CO_2*^-(ads) + H^+ + e^- \rightarrow HCOO*^-(ads)$ Step (3)

$HCOO*^-(ads) \rightarrow HCOO^-(aq)$ Step (4)

In the first step, CO_2 dissolves in the electrolyte and adsorbs on the electrocatalyst surface. Next, adsorbed $CO_2*^-(ads)$ (the asterisk * indicates the active site) is formed via a one-electron transfer (step (2)). $CO_2*^-(ads)$ is subsequently reduced and protonated in step (3) to form adsorbed $HCOO*^-$ ($HCOO*^-(ads)$), and formate is produced in step (4) by desorption of $HCOO*^-(ads)$.

To have a better understanding of the underlying mechanism of formate formation in CO_2RR for various Bi-based HFGDEs, the Tafel slope (slope of cathode potential vs. log of formate partial current density) can be used to analyze the kinetics of the CO_2-to-formate conversion. For each point, the tests were repeated at least three times with the standard deviations shown in Fig. 5d. t-test was done on Tafel slopes yielding a P-value of 0.002, indicating the great statistical difference among the set of data for each sample. It is known that with a Tafel slope of 118 mV dec^{-1}, the rate-limiting step during CO_2RR is the initial one-electron transfer step (step (2)) [45]. While, a Tafel slope of 59 mV dec^{-1} is indicative of a fast pre-equilibrium (step (2)), but slower reduction-protonation of $CO_2*^-(ads)$ (step (3)) [46]. For the case of CuBi-CE and CuBi-PE HFGDEs, the Tafel slopes were 131 and 113 mV dec^{-1} (Fig. 5d), respectively, closer to the theoretical value of 118 mV dec^{-1} than 59 mV dec^{-1}. This suggests that the initial one-electron transfer (step (2)) is the rate-limiting step of formation generation during CO_2RR [45].

For $CuBi_2O_3$-PE HFGDE, the Tafel slope decreased to 87 mV dec^{-1}, indicating a more rapid initial electron transfer of CO_2 molecule to form CO_2^{*-}(ads), and the rate-limiting step was transferred to the slower chemical reaction of CO_2^{*-} to form $HCOO^{*-}$ [47, 48]. This is in accordance with density functional theory calculations done on Bi and Bi_2O_3 elsewhere [33], which confirmed the facilitated adsorption of CO_2 on Bi_2O_3 than Bi, owing to the presence of Bi-O structure [49]. Therefore, the enhanced Bi-O structure helped to stabilize CO_2^{*-} intermediates and switched the rate-limiting step to the hydrogenation (step 3). A similar trend in Tafel slope (from around 120 to 85 mV dec^{-1}) was observed for Bi-based electrocatalysts containing high-valence Bi with carbonate species ($Bi_2O_2CO_3$). It showed an improved performance compared with pristine Bi [47, 48]. In addition, the decreased Tafel slope of HFGDEs with nanosheets (CuBi-PE and $CuBi_2O_3$-PE) as compared with CuBi-CE represents the intrinsic higher catalytic activity of nanosheets for CO_2RR to formate [36, 50]. The lower Tafel slope of $CuBi_2O_3$-PE HFGDE indicates the higher CO_2RR rate with increasing potential, which is beneficial for practical application [37], and it indicates that the strategy of using Bi_2O_3 nanosheets to improve catalyst performance is successful. These results were also in accordance with EIS analysis which exhibited a lower barrier of charge transfer and accelerated equilibrium of the first electron transfer on $CuBi_2O_3$-PE HFGDE [51] (Fig. 4c), resulting in switching the rate-determining step to the hydrogenation step [25].

3.3. HFGDE Durability and Comparison with Conventional GDEs

It is well known that long-term operation of HFGDEs is susceptible to performance drop when the HFGDEs are tested in a non-flow batch mode operation, due to the changes of pH, temperature, or ion concentration, which may influence the total efficiency [52]. It has been observed that the buildup of diffusion barriers led to decreased availability of CO_2 and bicarbonate at the electrode surface in an H-cell, resulting in a drop in the efficiency of the indium catalyst after a few hours

[53]. Herein, the HFGDE with the optimal performance ($CuBi_2O_3$-PE) was tested in a custom-made flow-type reactor (Fig. S16). The conventional flow-type GDE reactors usually use alkaline electrolytes to benefit from the lower ohmic resistance and significantly suppressed hydrogen evolution in alkaline electrolytes [43, 54]. In this case, CO_2 is supplied to the chamber via flow-by configuration, meaning that CO_2 flows alongside the GDE and it diffuses through the GDE by diffusion to minimize the reaction between alkaline and CO_2 [55]. However, for the case of HFGDEs, CO_2 is dissolved through the electrolyte (equivalent to the flow-through configuration of planar GDEs [55]). Therefore, alkaline electrolytes are not the optimal choice due to reaction with CO_2, and the same electrolyte (0.5M $KHCO_3$) is used for the flow-type cell. CO_2RR on $CuBi_2O_3$-PE HFGDE over 24 h operation at -1 V vs. RHE showed a stable operation with regard to faradaic efficiency and partial current density of formate (Fig. 5e). In addition, the formate partial current density achieved in the flow-cell (125-130 mA cm^{-2}) was higher than that achieved in the batch mode, due to the improved mass transport and reduced bicarbonate concentration polarization in the vicinity of the HFGDEs.

After CO_2RR, Bi_2O_3-rich surface is converted to Bi-rich materials due to partial reduction of Bi-oxide, as seen in the post-CO_2RR XRD pattern (Fig. S17a); however Bi-O structure remained after the electrolysis (Fig. S12d) and acted as the prime inducement for selective conversion of CO_2 to formate. Although some studies reported the complete reduction of Bi_2O_3 to Bi during CO_2RR according to the Pourbaix diagram [56], recent studies have shown the existence of Bi-O structure during electrolysis using advanced in-situ characterizations [33, 49, 57]. The kinetically-hindered reduction of Bi-oxide to Bi is due to the defect-rich nanostructured morphologies. This leads to the existence of metastable oxide valence in the structure, similar to other oxide-derived catalysts, such as Sn [45]. In addition, better performance of oxide-derived Bi as compared with Bi and the importance of Bi/Bi_2O_3 co-existence for formate formation have been reported in the literature

[22, 25]. This was found to be due to the highly defective surface and exitance of many low-coordination sites. These results are consistent with the results of this study.

Moreover, the Bi-based HFGDEs maintained their crystalline structure after CO_2RR (Fig. S12b, S11c, and S12d). Therefore, defect-rich nanosheets comprising Bi and Bi_2O_3 junction remained after the reduction, leading to a stable high current density of CO_2RR [25]. Post-CO_2RR XPS (Fig. S17 b, c, and d) exhibited no significant changes of Cu and $CuBi_2O_3$ HFGDEs, indicating the chemical stability HFGDEs during electrolysis. SEM images of the Bi_2O_3 nanosheets showed only slight damages in nanosheets (Fig. S18), and were still vertically aligned covering Cu HFGDE, therefore so significant changes for the performance were seen.

The HFGDE design reduces the cell complexity as CO_2 is supplied through the fiber lumen, without requiring to have a gas chamber, unlike conventional planar GDEs (Fig. S16). In addition, by using multiple HFGDEs or fabrication of HFGDEs with a smaller diameter, the electrode surface area and the ratio of surface area to volume of the cathode can be maximized (Fig. S16c). The operation of HFGDEs in a flow-type reactor for the first time in this study indicates the potential of HFGDEs for scaling-up gas electrolyzers working with aqueous electrolytes. Compared to other Bi-based catalysts used in an H-cell or Bi-based GDE used in flow-type reactors with aqueous electrolyte, the results of the HFGDEs here with vertically aligned Bi-based nanosheets outperform other Bi-based GDEs in similar testing conditions and electrolytes, as can be seen in Fig. 5f and Table S1. Advanced Bi-based electrodes with tuned nanostructure show FEs as high as 95-100% towards formate but suffer from low current density (Fig. 5f). Bi-based HFGDEs present a better performance as compared with CuSn HFGDEs, developed in our previous study [14], with a 0.2 V less overpotential, owing to the shape of nanosheets with the rough surface after oxidation in air, and introduction of stable Bi-O structure to enhance formate

generation mechanism. It should be noted that the studies with higher current density in aqueous media have employed alkaline electrolytes [58] or higher concentrations of $KHCO_3$ [20, 22], therefore the electron transfer resistance is substantially decreased and higher current densities can be achieved. The results here confirm that by the synergy of using unique shape HFGDEs and shape-controlled growth of formate-selective electrocatalysts, efficient and stable CO_2RR to formate in a bicarbonate electrolyte can be achieved at near commercially-relevant rates.

4. Conclusion

In this study, advanced HFGDEs equipped with shape-tuned and wettability-enhanced Bi-based electrocatalyst were prepared via pulse electrodeposition to facilitate the formation and regulation of triple-phase reaction sites for CO_2RR to formate. Pulse electrodeposition can replenish Bi^{3+} ions to the diffusion layer in the vicinity of the HFGDE, leading to a uniform growth of vertically aligned nanosheets which completely cover the Cu HFGDE. The HFGDE covered by Bi nanosheets offered much higher catalytic active sites with less catalyst loading, resulting in substantially higher mass activity as compared with the bulky shape layer obtained via continuous electrodeposition. The surface wettability of the catalyst layer was furthermore improved via oxidation at 220 °C, which introduced oxidation-induced defect sites and consequently contributed to more efficient formate production by switching the rate-limiting step to the hydrogenation step. This resulted in a current density of 141 mA cm^{-2} at -1 V vs. RHE with formate FE of 85%, outperforming the conventional planar Bi-based GDEs used for CO_2RR to formate in bicarbonate electrolytes. The post-CO_2RR analysis confirmed the simultaneous presence of metal and metal oxide in nanosheet structure, verifying the stability of induced oxides, consistent with the performance during stable long-term electrolysis tests. This study exhibited the substantial effects of surface wettability and catalyst nanostructure on the electrocatalytic efficiency and offers an

efficient method to enhance multiple phase interface formation and solve the issue of mass transfer in aqueous electrochemical reactions with a gas-fed reactant.

Supporting Information

The following information is presented in SI: images of HFGDEs and flow-type reactor, material characterization (TEM, SEM, EDX, XRD, XPS, and contact angle), and additional CO_2 electrolysis performance.

Conflict of Interest

The authors declare no conflict of interest.

Acknowledgments

The authors are thankful to the AWMC Analytical Services Laboratory (ASL) for HPLC analysis. This research was funded through Laureate Fellowship FL170100086 by the Australian Research Council (ARC), awarded to Professor Zhiguo Yuan. H.R. is supported by The University of Queensland (UQ) Research Training Scholarship. X.Z. is supported by UQ International Scholarship (UQI). We acknowledge the support from the Centre for Microscopy and Microanalysis (CMM) at UQ (SEM, TEM, XRD, and XPS analyses). This work was performed in part at the Queensland node of the Australian National Fabrication Facility. A company established under the National Collaborative Research Infrastructure Strategy to provide nano and microfabrication facilities for Australia's researchers.

References

[1] P. De Luna, C. Hahn, D. Higgins, S.A. Jaffer, T.F. Jaramillo, E.H. Sargent, What would it take for renewably powered electrosynthesis to displace petrochemical processes?, Science, 364 (2019).

[2] M.T. Tang, H. Peng, P.S. Lamoureux, M. Bajdich, F. Abild-Pedersen, From electricity to fuels: Descriptors for C1 selectivity in electrochemical CO2 reduction, Appl. Catal. B, 279 (2020).
[3] H. Xiang, H.A. Miller, M. Bellini, H. Christensen, K. Scott, S. Rasul, E.H. Yu, Production of formate by CO2 electrochemical reduction and its application in energy storage, Sustain Energ Fuels, 4 (2020) 277-284.
[4] R. Hegner, L.F.M. Rosa, F. Harnisch, Electrochemical CO2 reduction to formate at indium electrodes with high efficiency and selectivity in pH neutral electrolytes, Appl. Catal. B, 238 (2018) 546-556.
[5] M. Li, S. Garg, X. Chang, L. Ge, L. Li, M. Konarova, T.E. Rufford, V. Rudolph, G. Wang, Toward Excellence of Transition Metal-Based Catalysts for CO2 Electrochemical Reduction: An Overview of Strategies and Rationales, Small Methods, 4 (2020) 2000033-2000063.
[6] T. Burdyny, W.A. Smith, CO2 Reduction on Gas-Diffusion Electrodes and Why Catalytic Performance Must Be Assessed at Commercially-relevant Conditions, Energy Environ. Sci., 12 (2019) 1442-1453.
[7] X. Zhang, T. Lei, Y. Liu, J. Qiao, Enhancing CO2 electrolysis to formate on facilely synthesized Bi catalysts at low overpotential, Appl. Catal. B, 218 (2017) 46-50.
[8] S. Garg, M.R. Li, A.Z. Weber, L. Ge, L.Y. Li, V. Rudolph, G.X. Wang, T.E. Rufford, Advances and challenges in electrochemical CO2 reduction processes: an engineering and design perspective looking beyond new catalyst materials, J. Mater. Chem. A, 8 (2020) 1511-1544.
[9] Z. Bitar, A. Fecant, E. Trela-Baudot, S. Chardon-Noblat, D. Pasquier, Electrocatalytic Reduction of Carbon Dioxide on Indium Coated Gas Diffusion Electrodes-Comparison with Indium Foil, Appl. Catal. B, 189 (2016) 172-180.
[10] Y.C. Tan, K.B. Lee, H. Song, J. Oh, Modulating Local CO2 Concentration as a General Strategy for Enhancing C−C Coupling in CO2 Electroreduction, Joule, 4 (2020) 1104-1120.
[11] R. Shi, J. Guo, X. Zhang, G.I.N. Waterhouse, Z. Han, Y. Zhao, L. Shang, C. Zhou, L. Jiang, T. Zhang, Efficient wettability-controlled electroreduction of CO2 to CO at Au/C interfaces, Nat. Commun., 11 (2020) 3028-3037.
[12] M.E. Leonard, L.E. Clarke, A. Forner-Cuenca, S.M. Brown, F.R. Brushett, Investigating Electrode Flooding in a Flowing Electrolyte, Gas-Fed Carbon Dioxide Electrolyzer, ChemSusChem, 13 (2020) 400-411.
[13] Y. Chen, N.S. Lewis, C. Xiang, Modeling the Performance of A Flow-Through Gas Diffusion Electrode for Electrochemical Reduction of CO or CO2, J. Electrochem. Soc., 167 (2020).
[14] H. Rabiee, X. Zhang, L. Ge, S. Hu, M. Li, S. Smart, Z. Zhu, Z. Yuan, Tuning the Product Selectivity of the Cu Hollow Fiber Gas Diffusion Electrode for Efficient CO2 Reduction to Formate by Controlled Surface Sn Electrodeposition, ACS Appl. Mater. Interfaces, 12 (2020) 21670-21681.
[15] R. Kas, K.K. Hummadi, R. Kortlever, P. de Wit, A. Milbrat, M.W. Luiten-Olieman, N.E. Benes, M.T. Koper, G. Mul, Three-dimensional Porous Hollow Fibre Copper Electrodes for Efficient and High-rate Electrochemical Carbon Dioxide Reduction, Nat. Commun., 7 (2016) 10748-10754.
[16] X. Zhang, J. Fu, Y. Liu, X.-D. Zhou, J. Qiao, Bismuth Anchored on MWCNTs with Controlled Ultrafine Nanosize Enables High-Efficient Electrochemical Reduction of Carbon Dioxide to Formate Fuel, ACS Sustain. Chem. Eng., 8 (2020) 4871-4876.
[17] M. Fan, S. Prabhudev, S. Garbarino, J. Qiao, G.A. Botton, D.A. Harrington, A.C. Tavares, D. Guay, Uncovering the nature of electroactive sites in nano architectured dendritic Bi for highly efficient CO2 electroreduction to formate, Appl. Catal. B, 274 (2020) 119031-119039.
[18] S. Kim, W.J. Dong, S. Gim, W. Sohn, J.Y. Park, C.J. Yoo, H.W. Jang, J.-L. Lee, Shape-controlled bismuth nanoflakes as highly selective catalysts for electrochemical carbon dioxide reduction to formate, Nano Energy, 39 (2017) 44-52.
[19] A. Dutta, M. Rahaman, N.C. Luedi, M. Mohos, P. Broekmann, Morphology Matters: Tuning the Product Distribution of CO2 Electroreduction on Oxide-Derived Cu Foam Catalysts, ACS Catal., 6 (2016) 3804-3814.
[20] F.P. Garcia de Arquer, O.S. Bushuyev, P. De Luna, C.T. Dinh, A. Seifitokaldani, M.I. Saidaminov, C.S. Tan, L.N. Quan, A. Proppe, M.G. Kibria, S.O. Kelley, D. Sinton, E.H. Sargent, 2D Metal Oxyhalide-Derived Catalysts for Efficient CO2 Electroreduction, Adv. Mater., 30 (2018) 1802858-1802863.
[21] M. Zhao, Y. Gu, W. Gao, P. Cui, H. Tang, X. Wei, H. Zhu, G. Li, S. Yan, X. Zhang, Z. Zou, Atom vacancies induced electron-rich surface of ultrathin Bi nanosheet for efficient electrochemical CO2 reduction, Appl. Catal. B, 266 (2020) 118625-118632.
[22] Q. Gong, P. Ding, M. Xu, X. Zhu, M. Wang, J. Deng, Q. Ma, N. Han, Y. Zhu, J. Lu, Z. Feng, Y. Li, W. Zhou, Y. Li, Structural defects on converted bismuth oxide nanotubes enable highly active electrocatalysis of carbon dioxide reduction, Nat. Commun., 10 (2019) 2807-2816.
[23] Q. Wang, Y. Lei, D. Wang, Y. Li, Defect engineering in earth-abundant electrocatalysts for CO2 and N2 reduction, Energy Environ. Sci., 12 (2019) 1730-1750.

[24] X. Zhang, Z. Chen, M. Jiao, X. Ma, K. Mou, F. Cheng, Z. Wang, X. Zhang, L. Liu, Defects and Conductive Nitrogen-Carbon Framework Regulated ZnInOx Nanosheets for Boosting CO2 Electrocatalytic Reduction, Appl. Catal. B, 279 (2020) 119383-119389.
[25] D. Wu, G. Huo, W. Chen, X.-Z. Fu, J.-L. Luo, Boosting formate production at high current density from CO2 electroreduction on defect-rich hierarchical mesoporous Bi/Bi2O3 junction nanosheets, Appl. Catal. B, 271 (2020) 118957-118964.
[26] S. Liu, Z. Luo, J. Guo, A. Pan, Z. Cai, S. Liang, Bismuth nanosheets grown on carbon fiber cloth as advanced binder-free anode for sodium-ion batteries, Electrochem. Commun., 81 (2017) 10-13.
[27] S. Zhang, P. Kang, T.J. Meyer, Nanostructured Tin Catalysts for Selective Electrochemical Reduction of Carbon Dioxide to Formate, J. Am. Chem. Soc., 136 (2014) 1734-1737.
[28] Q. Wu, P. Diao, J. Sun, T. Jin, D. Xu, M. Xiang, Electrodeposition of Vertically Aligned Silver Nanoplate Arrays on Indium Tin Oxide Substrates, J. Phys. Chem. C, 119 (2015) 20709-20720.
[29] X.W. An, S.S. Li, A. Yoshida, Z.D. Wang, X.G. Hao, A. Abudula, G.Q. Guan, Electrodeposition of Tin-Based Electrocatalysts with Different Surface Tin Species Distributions for Electrochemical Reduction of CO2 to HCOOH, ACS Sustain. Chem. Eng., 7 (2019) 9360-9368.
[30] Q.N. Wang, C.Q. Zhu, C. Wu, H.B. Yu, Direct synthesis of bismuth nanosheets on a gas diffusion layer as a high-performance cathode for a coupled electrochemical system capable of electroreduction of CO2 to formate with simultaneous degradation of organic pollutants, Electrochim. Acta, 319 (2019) 138-147.
[31] Y. Hinuma, T. Toyao, T. Kamachi, Z. Maeno, S. Takakusagi, S. Furukawa, I. Takigawa, K.-i. Shimizu, Density Functional Theory Calculations of Oxygen Vacancy Formation and Subsequent Molecular Adsorption on Oxide Surfaces, J. Phys. Chem. C, 122 (2018) 29435-29444.
[32] F.Y. Gao, S.J. Hu, X.L. Zhang, Y.R. Zheng, H.J. Wang, Z.Z. Niu, P.P. Yang, R.C. Bao, T. Ma, Z. Dang, Y. Guan, X.S. Zheng, X. Zheng, J.F. Zhu, M.R. Gao, S.H. Yu, High-Curvature Transition-Metal Chalcogenide Nanostructures with a Pronounced Proximity Effect Enable Fast and Selective CO2 Electroreduction, Angew. Chem., 132 (2020) 8784-8790.
[33] P. Deng, H. Wang, R. Qi, J. Zhu, S. Chen, F. Yang, L. Zhou, K. Qi, H. Liu, B.Y. Xia, Bismuth Oxides with Enhanced Bismuth–Oxygen Structure for Efficient Electrochemical Reduction of Carbon Dioxide to Formate, ACS Catal., 10 (2019) 743-750.
[34] T. Sarkar, S. Ghosh, M. Annamalai, A. Patra, K. Stoerzinger, Y.-L. Lee, S. Prakash, M.R. Motapothula, Y. Shao-Horn, L. Giordano, T. Venkatesan, The effect of oxygen vacancies on water wettability of transition metal based SrTiO3 and rare-earth based Lu2O3, Rsc Adv, 6 (2016) 109234-109240.
[35] V.-H. Castrejón-Sánchez, A.C. Solís, R. López, C. Encarnación-Gomez, F.M. Morales, O.S. Vargas, J.E. Mastache-Mastache, G.V. Sánchez, Thermal oxidation of copper over a broad temperature range: towards the formation of cupric oxide (CuO), Mater. Res. Express, 6 (2019) 75909.
[36] D.B. Zhang, Z.T. Tao, F.L. Feng, B.B. He, W. Zhou, J. Sun, J.M. Xu, Q. Wang, L. Zhao, High efficiency and selectivity from synergy: Bi nanoparticles embedded in nitrogen doped porous carbon for electrochemical reduction of CO2 to formate, Electrochim. Acta, 334 (2020) 135563.
[37] F. Lei, W. Liu, Y. Sun, J. Xu, K. Liu, L. Liang, T. Yao, B. Pan, S. Wei, Y. Xie, Metallic tin quantum sheets confined in graphene toward high-efficiency carbon dioxide electroreduction, Nat. Commun., 7 (2016) 12697-12704.
[38] X. Zhang, X. Sun, S.-X. Guo, A.M. Bond, J. Zhang, Formation of lattice-dislocated bismuth nanowires on copper foam for enhanced electrocatalytic CO2 reduction at low overpotential, Energy Environ. Sci., 12 (2019) 1334-1340.
[39] N. Gutiérrez-Guerra, L. Moreno-López, J.C. Serrano-Ruiz, J.L. Valverde, A. de Lucas-Consuegra, Gas phase electrocatalytic conversion of CO 2 to syn-fuels on Cu based catalysts-electrodes, Appl. Catal. B, 188 (2016) 272-282.
[40] H. Zhang, Y. Ma, F. Quan, J. Huang, F. Jia, L. Zhang, Selective electro-reduction of CO2 to formate on nanostructured Bi from reduction of BiOCl nanosheets, Electrochem. Commun., 46 (2014) 63-66.
[41] J. Greeley, T.F. Jaramillo, J. Bonde, I.B. Chorkendorff, J.K. Norskov, Computational High-throughput Screening of Electrocatalytic Materials for Hydrogen Evolution, Nat. Mater., 5 (2006) 909-913.
[42] Y. Hori, Electrochemical CO2 Reduction on Metal Electrodes, in: C. Vayenas (Ed.) Electrochemical CO2 Reduction on Metal Electrodes, Springer, New York, USA, 2008, pp. 89-189.
[43] F.P. Garcia de Arquer, C.T. Dinh, A. Ozden, J. Wicks, C. McCallum, A.R. Kirmani, D.H. Nam, C. Gabardo, A. Seifitokaldani, X. Wang, Y.C. Li, F. Li, J. Edwards, L.J. Richter, S.J. Thorpe, D. Sinton, E.H. Sargent, CO2 electrolysis to multicarbon products at activities greater than 1 A cm(-2), Science, 367 (2020) 661-666.
[44] B. Kim, H. Seong, J.T. Song, K. Kwak, H. Song, Y.C. Tan, G. Park, D. Lee, J. Oh, Over a 15.9% Solar-to-CO Conversion from Dilute CO2 Streams Catalyzed by Gold Nanoclusters Exhibiting a High CO2 Binding Affinity, ACS Energy Lett., 5 (2019) 749-757.

[45] Y. Chen, M.W. Kanan, Tin Oxide Dependence of the CO2 Reduction Efficiency on Tin Electrodes and Enhanced Activity for Tin/Tin Oxide Thin-film Catalysts, J. Am. Chem. Soc., 134 (2012) 1986-1989.
[46] M. Dunwell, W. Luc, Y. Yan, F. Jiao, B. Xu, Understanding Surface-Mediated Electrochemical Reactions: CO2 Reduction and Beyond, ACS Catal., 8 (2018) 8121-8129.
[47] X. An, S. Li, X. Hao, X. Du, T. Yu, Z. Wang, X. Hao, A. Abudula, G. Guan, The in situ morphology transformation of bismuth-based catalysts for the effective electroreduction of carbon dioxide, Sustainable Energy & Fuels, 4 (2020) 2831-2840.
[48] W. Lv, J. Bei, R. Zhang, W. Wang, F. Kong, L. Wang, W. Wang, Bi2O2CO3 Nanosheets as Electrocatalysts for Selective Reduction of CO2 to Formate at Low Overpotential, ACS Omega, 2 (2017) 2561-2567.
[49] F. Li, G.H. Gu, C. Choi, P. Kolla, S. Hong, T.-S. Wu, Y.-L. Soo, J. Masa, S. Mukerjee, Y. Jung, J. Qiu, Z. Sun, Highly stable two-dimensional bismuth metal-organic frameworks for efficient electrochemical reduction of CO2, Appl. Catal. B, 277 (2020) 119241-119250.
[50] A. Wuttig, Y. Yoon, J. Ryu, Y. Surendranath, Bicarbonate Is Not a General Acid in Au-Catalyzed CO2 Electroreduction, J. Am. Chem. Soc., 139 (2017) 17109-17113.
[51] Q. Li, X. Zhang, X. Zhou, Q. Li, H. Wang, J. Yi, Y. Liu, J. Zhang, Simply and effectively electrodepositing Bi-MWCNT-COOH composite on Cu electrode for efficient electrocatalytic CO2 reduction to produce HCOOH, J. CO2 Util., 37 (2020) 106-112.
[52] S. Garg, M. Li, T.E. Rufford, L. Ge, V. Rudolph, R. Knibbe, M. Konarova, G.G.X. Wang, Catalyst-Electrolyte Interactions in Aqueous Reline Solutions for Highly Selective Electrochemical CO2 Reduction, ChemSusChem, 13 (2020) 304-311.
[53] S.R. Narayanan, B. Haines, J. Soler, T.I. Valdez, Electrochemical Conversion of Carbon Dioxide to Formate in Alkaline Polymer Electrolyte Membrane Cells, J. Electrochem. Soc., 158 (2011) A167-A173.
[54] H. Xiang, S. Rasul, B. Hou, J. Portoles, P. Cumpson, E.H. Yu, Copper-Indium Binary Catalyst on a Gas Diffusion Electrode for High-Performance CO2 Electrochemical Reduction with Record CO Production Efficiency, ACS Appl. Mater. Interfaces, 12 (2020) 601-608.
[55] M. Duarte, B. De Mot, J. Hereijgers, T. Breugelmans, Electrochemical Reduction of CO2: Effect of Convective CO2 Supply in Gas Diffusion Electrodes, ChemElectroChem, 6 (2019) 5596-5602.
[56] J.E. Pander, D. Ren, Y. Huang, N.W.X. Loo, S.H.L. Hong, B.S. Yeo, Understanding the Heterogeneous Electrocatalytic Reduction of Carbon Dioxide on Oxide-Derived Catalysts, ChemElectroChem, 5 (2018) 219-237.
[57] C.W. Lee, J.S. Hong, K.D. Yang, K. Jin, J.H. Lee, H.-Y. Ahn, H. Seo, N.-E. Sung, K.T. Nam, Selective Electrochemical Production of Formate from Carbon Dioxide with Bismuth-Based Catalysts in an Aqueous Electrolyte, ACS Catal., 8 (2018) 931-937.
[58] G. Díaz-Sainz, M. Alvarez-Guerra, J. Solla-Gullón, L. García-Cruz, V. Montiel, A. Irabien, CO2 Electroreduction to Formate: Continuous Single-pass Operation in a Filter-press Reactor at High Current Densities Using Bi Gas Diffusion Electrodes, J. CO2 Util., 34 (2019) 12-19.